Nanoscale

PAPER

Cite this: *Nanoscale*, 2015, **7**, 5776

"Crystallographic" holes: new insights for a beneficial structural feature for photocatalytic applications†

Krisztina Vajda,[a] Zsolt Kása,[a] András Dombi,[a] Zoltán Németh,[b] Gábor Kovács,[c,d] Virginia Danciu,[c] Teodora Radu,[d,e] Corneliu Ghica,[f] Lucian Baia,[d,e] Klára Hernádi[a,b] and Zsolt Pap*[a,c,d]

Received 4th December 2014,
Accepted 18th February 2015

DOI: 10.1039/c4nr07157c

www.rsc.org/nanoscale

One of the most fundamental aspects of the heterogeneous catalysis field is the manipulation of the catalysts' activity. In photocatalysis this is carried out by maximizing the right crystal plane of a semiconductor oxide. Until now, most of the papers have achieved this by a combination of different oxides, with noble metals and sometimes with carbon nanomaterials. In this work MWCNTs (multiwalled carbon nanotubes) were applied as "crystallization promoters" in a very simple, safe, one-step hydrothermal method. By this method TiO_2 nano/micro crystals with exposed {001} facets were obtained in the first step. The next episode in the crystal manipulation "saga" was the modification of the (001) crystallographic plane's structure by creating ordered/own faceted "crystallographic holes". These elements are capable of further enhancing the obtained activity of titania microcrystals to a higher extent, as shown by the UV driven photocatalytic phenol degradation experiments. The appearance of the holes was "provoked" by simple calcination and their presence and influence were demonstrated by XPS and HRTEM.

Introduction

TiO_2 has been a widely investigated semiconductor photocatalyst material over the last 2–3 decades. As is very well-known, the crystalline structure and surface chemistry (the presence of different crystal phases, porosity, surface groups, oxidation states and the chemical environment of the surface atoms,[1,2] shape of the crystallites[3]) of TiO_2 are significant factors that affects photocatalytic performance.

It is known that the anatase phase shows better photocatalytic activity than rutile, because of the low recombination rate of photo-generated electrons, and holes.[4,5] That is why one of the structural parameters, which has gained high interest in the last few years, was the shape manipulation of anatase TiO_2 crystallites at nano- and micro-scales. Usually, the anatase TiO_2 crystals are dominated by the thermodynamically stable {101} crystal planes, rather than the much more reactive {001} facets. Consequently, the researchers in the field tried to synthesize uniform anatase TiO_2 single crystals with a high percentage of {001} crystallographic planes. Moreover, it was found that by adjusting the crystallographic planes' ratio *e.g.* (001), (101) the photocatalytic activity was critically influenced.[6] Hence, the appearance of applications (such as photoelectrodes made from nanocrystalline {001} facet dominated TiO_2 and carbon aerogel) and in-depth investigations was inevitable regarding this issue.

As already stated, much effort has been focused on developing new routes for preparing {001} facets dominated anatase TiO_2 single crystals.[3,7–17] There are different synthesis paths to produce TiO_2 crystals, such as trough titanate nanotubes (TNTs) in supercritical water. The transformation of the TNTs into anatase nanocrystals was achieved by two simultaneous processes (dissolution–nucleation and crystal growth while the other is an *in situ* nucleation and crystal growth).[18] Other synthesis approaches used a water-2-propanol solvothermal synthetic route, during which high-quality anatase TiO_2 single-crystal nanosheets with 64% {001} facets[12] were obtained. Interesting synthesis methods were developed based on the

---

[a] *Research Group of Environmental Chemistry, University of Szeged, Tisza Lajos krt. 103, H-6720 Szeged, Hungary. E-mail: k.hernadi@chem.u-szeged.hu, pzsolt@chem.u-szeged.hu*

[b] *Department of Applied and Environmental Chemistry, University of Szeged, Rerrich tér 1, H-6720 Szeged, Hungary*

[c] *Faculty of Chemistry and Chemical Engineering, Babeş-Bolyai University, Arany János 11, RO-400028 Cluj-Napoca, Romania*

[d] *Faculty of Physics, Babeş-Bolyai University, M. Kogălniceanu 1, RO-400084 Cluj-Napoca, Romania*

[e] *Institute for Interdisciplinary Research on Bio-Nano-Sciences, Treboniu Laurian 42, RO-400271 Cluj-Napoca, Romania*

[f] *National Institute of Materials Physics, Atomistilor 105 b, RO-077125 Măgurele-Ilfov, Romania*

† Electronic supplementary information (ESI) available. See DOI: 10.1039/c4nr07157c

reaction of tetrabutyl titanate and HF, which resulted in nanosized anatase sheet-like TiO_2 single crystals with 89% of {001} facets exhibiting superior photocatalytic performance.[16] Both theoretical and experimental results indicate that because of the higher surface energy of {001} facets, these are more effective for dissociative adsorption of organics and more efficient in the generation of $^{\bullet}OH$ radicals compared with the thermodynamically more stable {101} facets.[19] Shape tailoring is not the only efficient way to modify the activity of titania photocatalysts. Among other approaches the "composite materials" strategy is continuously investigated and success stories are to be found in the literature, such as the combination of TiO_2 with other oxides (*e.g.* WO_3 [20]), noble metals (Au, Pt[21]) or even carbon materials (graphite, carbon nanotubes,[22] *etc.*). Usually, the main purpose of using composite material systems is their positive role in charge carrier dynamics[23,24] and the improvement in the affinity between anionic and cationic pollutants and the photocatalyst.[25] Every listed material above has specific parameters, which need tuning to achieve the desired end-product. This is the case of the functionalization of the carbon nanotubes, where the deposition methodology of TiO_2 influences the photocatalytic activity of the nanocomposites (the enhancement of the photocatalytic activity was supported by the more efficient electron transfer properties of the oxygen- than those of amino-containing functional groups, which support the efficient charge transportation and separation of the photogenerated electron–hole pairs).[26]

Strategically speaking it is possible to merge the composite materials approach with the shape controlling methodologies in order to obtain *in situ* grown composite materials. Thus, the main research thread of the present work was to obtain shape-controlled anatase titania microcrystals in the presence of carbon nanotubes in such a way that the semiconductor oxide crystallizes only in the presence of the applied carbon material. By this process it is guaranteed that the crystal growth of the first particles is seeded at the surface of the multi-walled carbon nanotubes (MWCNT), meaning that a "foreign material seeded" growth is assured.

Results and discussion

Research strategy followed throughout the present work

As presented in Fig. 1, a well-designed research strategy was charted. In the first instance the effect of the hydrothermal treatment time was followed in order to distinguish the evolution stages of the crystallites by applying the proposed synthesis methods. Several important aspects that followed throughout the present work were the formation of the nanoplates itself, the formation of facet (001), the formation of the other representative facets (*i.e.* (101)) and the overgrowth of the particles. These synthesis methods were chosen, while the microparticles' average size remained constant.

The key aspect of the research route was to obtain secondary structural features, the "crystallographic holes" using a simple one-step approach. The chosen and successfully applied method was the traditional calcination, which was applied after the hydrothermal treatment. The crystallization process and the holes orientation were the mainly followed research interests while observing their influence on the photocatalytic activity.

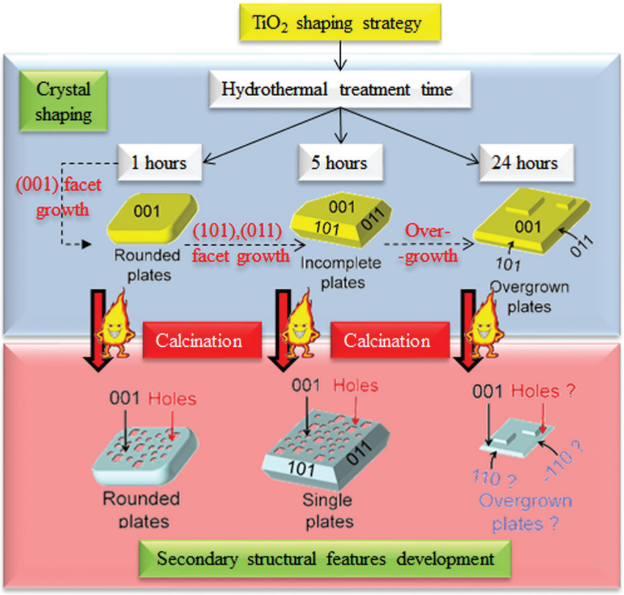

Fig. 1 The applied research strategy for the synthesis of titania nanoplates.

The role of the carbon nanotube as crystallization promoter

As emphasized in the previous section, the growth of these interesting materials occurs only in the presence of MWCNTs. In the first step (1), before the addition of MWCNTs, the precursor ($Ti(X)_4$, where X is any organic or inorganic group) undergoes a hydrolyzation reaction in strongly acidic media assured by the HCl and HF (details regarding the concentrations and amount of all the reactants can be found in the Experimental section):

$$Ti(X)_4 + yHOH \rightarrow Ti(OH)_y(X)_{4-y} + yH(X) \qquad (1)$$

Under these conditions, the hydrolysis product ($Ti(OH)_y(X)_{4-y}$, where $y = 2$ or 3[27]) is stable. In the presence of MWCNTs these compounds can adsorb on the provided surface (S_{MWCNT}) (2).

$$Ti(OH)_y(X)_{4-y} + S_{MWCNT} \rightarrow Ti(OH)_y(X)_{4-y} - S_{MWCNT} \qquad (2)$$

When the reaction mixture is transferred to the autoclave and heated to the desired temperature, the hydrolysis products start to decompose (3):

$$Ti(OH)_y(X)_{4-y} - S_{MWCNT} \rightarrow (4-y)HX + TiO_2 - S_{MWCNT} + (y-2)H_2O \qquad (3)$$

When the first crystallization germ appears at the surface of the MWCNTs, the crystal starts to grow. As the F^- ions are present under acidic conditions during this process, the anatase facet (001) is stabilized resulting in the TiO_2 nanoplates. If the MWCNT is missing from the reaction system, the TiO_2 growth is inhibited, as anatase is soluble in the presence of HF[28,29] (more precisely no crystallization germs are present).

Structural features of the obtained micro-materials

Morphological overview of the hydrothermally obtained titanias. The first aspect investigated was the influence of the hydrothermal treatment time. As shown in Fig. 2, in the case of shorter hydrothermal treatments (1 h), TiO_2 edgeless plates were obtained (sample NP-1H – please note that the sample nomenclature can be consulted in the Experimental section). Interestingly, only the {001} crystallographic plane was clearly formed, while the other facets were not. Moreover, rounded "planes" were observed, which did not show any specific orientation (all the facet-related information was based on the SAED patterns of the samples). This means that the crystallization process has not yet been completed.

The sample was monodisperse, meaning that the shape and size (≈1 μm) of all of the microparticles were the same. In the case of a 5 h hydrothermal treatment the boundaries between the mentioned facets appeared. However, a recrystallization process was clearly underway because of the plate fragments; incomplete plates (Fig. 2, sample NP-5H) were noticed in these samples, while the crystallite size still remained the same. When the hydrothermal treatment time was prolonged even more (24 h) the shape remained unchanged (Fig. 2, sample NP-24H) and in some cases twin crystals were also noticed. Taking into account the above findings one could infer that the crystals' morphology can be further evolved applying an additional crystallization step.

As reported and applied in many publications, a supplementary crystallization process, such as calcination, can improve the crystallinity grade[30,31] of the materials (*e.g.* to achieve higher photocatalytic activity), thus, the thermal treatment represents a simple, but efficient choice in the case of the materials investigated in the present work.

Morphological specificities on the microplates – the crystallographic holes – characterization and geometrical particularities. As the calcination was applied to the hydrothermally treated materials, the appearance of some interesting secondary structural features were noticed, such as holes (Fig. 3, samples NP-xH-C, $x = 1, 5, 24$ hours). At first sight, these holes could be characterized as shapes that are irregularly and randomly oriented throughout the microcrystalline material, and that seem to confer a porous sponge-like appearance to the crystal. Surprisingly, holes were formed in all investigated nanomaterials (1, 5 or 24 h), when thermal treatment was applied. Similar structures were obtained, originating from different synthesis procedures,[32,33] although to our knowledge none of them was investigated for photocatalytic purposes.

The HRTEM images (Fig. 4) revealed an interesting order of the holes throughout the plates. The observed high level order of the "crystallographic" holes clearly suggested that their formation mechanism is not related to the calcination specific phenomena at all, such as water/other organics loss (if that was the case, then volcano-like craters should have been observed as already shown in our recent papers, both at nano/macro scale[31,34]).

The most plausible explanation could be that the holes originate from a secondary recrystallization process that occurs during the heat treatment. It was observed in the NP-24H-C material that the marginal zones of the plates resemble more or less those of a biscuit. This suggests that material transfer occurred both during the hydrothermal treatment (suggested by the presence of small/big and twin plates) and during the calcination (very smooth/flawless plates before the heat treatment).

The above mentioned internal recrystallization process is also reinforced by the fact that it seems that the majority of the holes is the exact replica of the corresponding micrometric particle at nanometric scale. To examine more closely this issue 3D projections of the TEM images were evaluated. As shown in Fig. 5 the developed hole-like structures are nearly perfect squares at the centre of the microplates with slightly

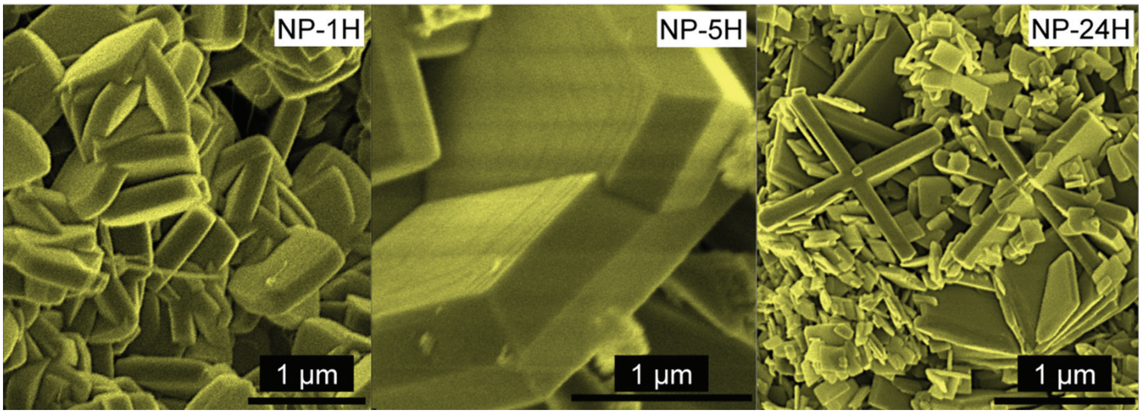

Fig. 2 The investigation of the hydrothermal treatment time's impact (1, 5 and 24 hours).

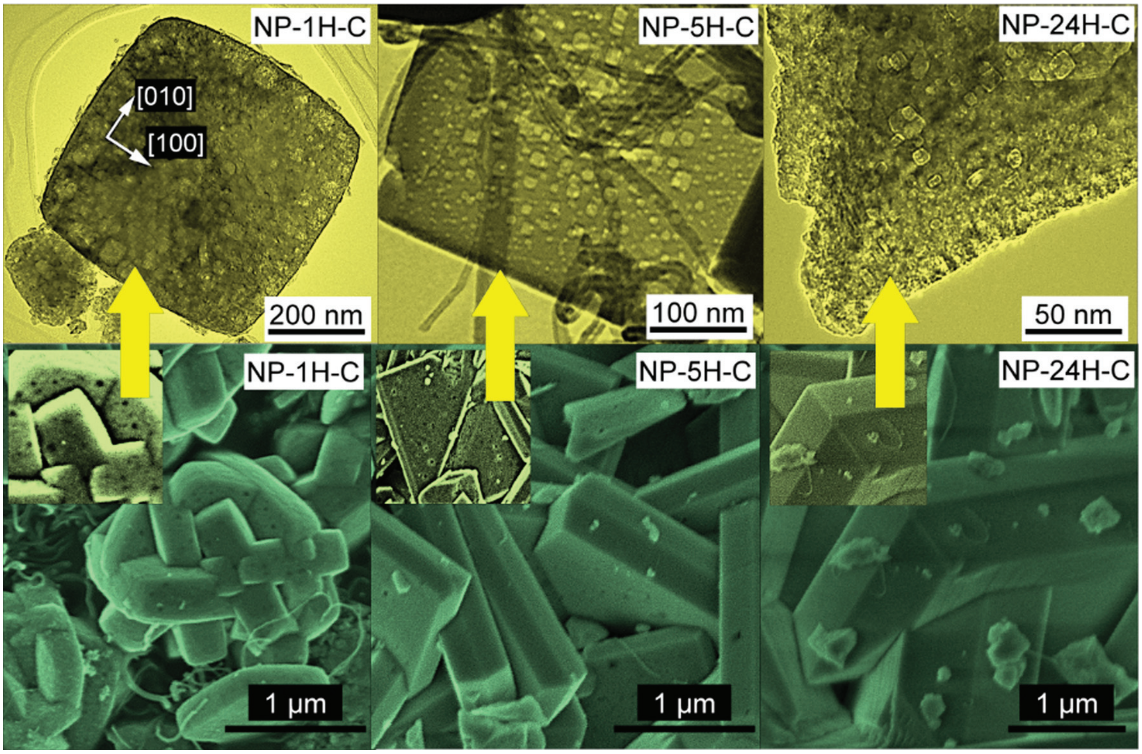

Fig. 3 The effect of the calcination (400 °C, 2 h in continuous air flow) on the hydrothermally treated TiO_2 photocatalysts – SEM micrographs (lower figure series) showing the appearance of the crystallographic holes. The upper row contains the TEM micrographs which reveals the arrangement of these structural features.

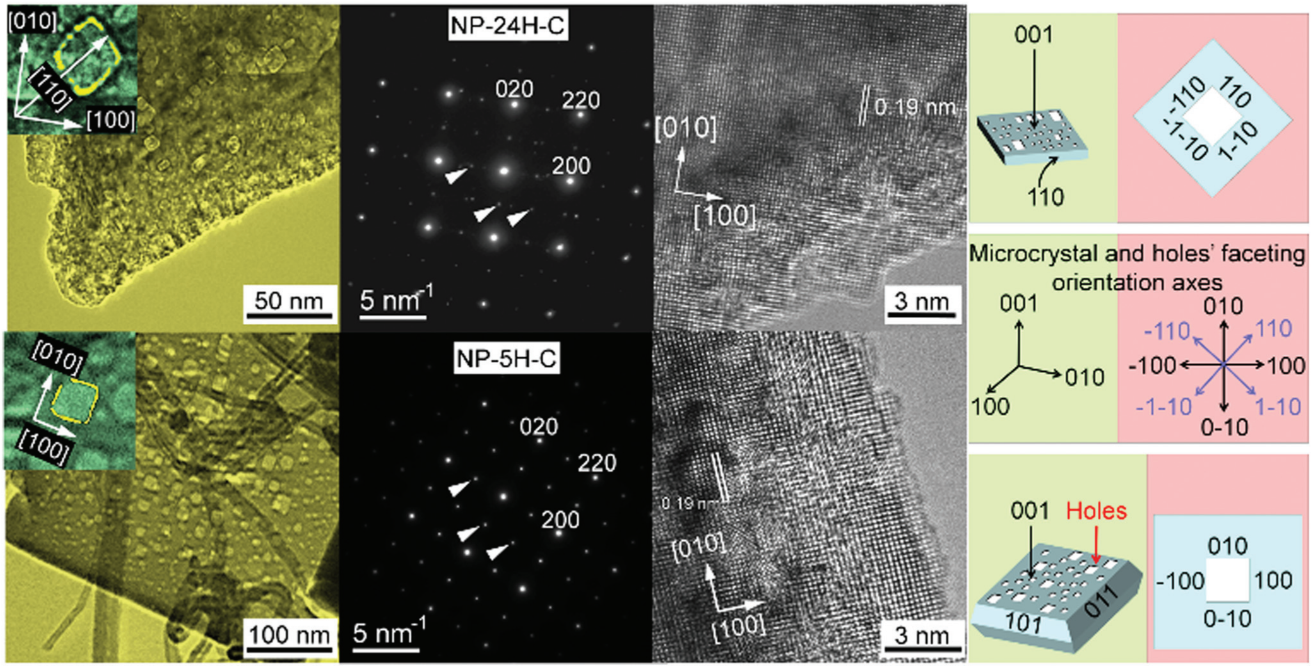

Fig. 4 The orientation of the crystallographic holes. Investigation at atomic level.

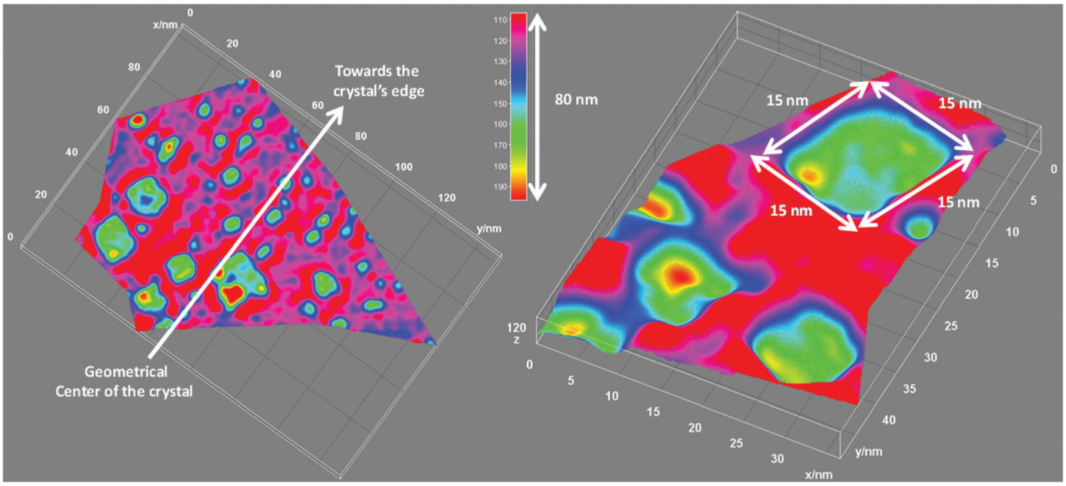

Fig. 5 3D projection of 2D TEM/HR-TEM images of sample NP-24H-C based on electron transmissibility. The rectangular shape of the larger holes is clearly visible, while the smaller ones tend to have rounded edges, taking circular shape at the edge of the microcrystal.

rounded corners and $d > 10$ nm, while the smaller entities ($d < 10$ nm) were mostly spherical.

The larger ones showed 50–80 nm depth, while the holes with smaller diameter were 30–60 nm deep.

This information can be connected with that of the microcrystallite thickness observed from the SEM micrographs, which were evaluated to be ≈100 nm. The walls of the crystallographic holes form a 90 degree angle with the particle surface and the bottom of the hole in a single step. The holes illustrated in Fig. 5 represent those which are near the centre of the particles. On examining other similar entities, it can be seen that their size gets smaller the nearer they are to the particles' edge. Together with their size decrease, the geometry of the holes changes gradually to the spherical (Fig. 5). Other size and shape distribution related statistics can be found in the ESI† (Fig. S1).

The maximum size of the holes was ≈20 nm, while the smallest ones were ≈5 nm. Their correlation with the geometrical positioning is illustrated in Fig. 6. The only exceptions to this observation was sample NP-1H-C, which was found to contain holes of random sizes dispersed throughout the entire particle.

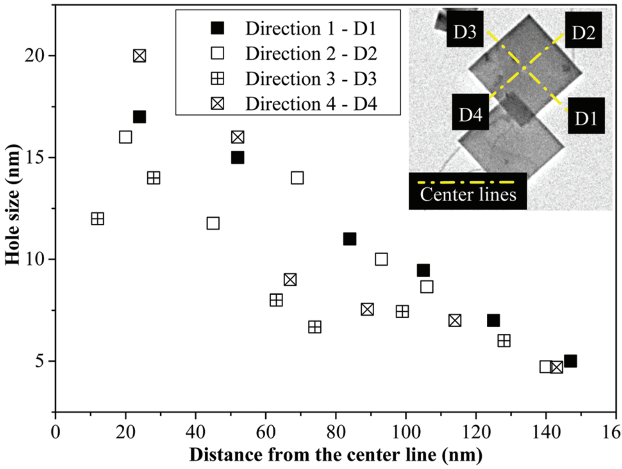

Fig. 6 The size variation of the crystallographic holes, measured from the center of the plates in 4 different directions (D1–D4). 25 particles were examined using this methodology, meaning for each point of the graph 25 size data and 25 distance data was available.

As stated previously, the holes were omnipresent in each of the calcined materials. Consequently, their orientation was examined at the atomic level and it was observed that in the case of sample NP-1H-C and NP-5H-C (Fig. 3) they were parallel with the crystallographic directions of [010] and [100], while in the case of NP-24H-C, they suffered a rotation and became parallel with the [110] direction.

If indeed that is the case, then the latter phenomenon should be a clear sign of a stabilization process (usually during the calcination procedure at a given temperature, the thermodynamically favoured crystal parameters should dominate the material – including size, shape and formation of different crystal phases/local structure modifications). To enlighten these aspects classical structural investigations were carried out to obtain indirect evidence about the presence of the holes and their rotation.

Structure of the obtained microplates and the influence of the crystallographic holes. The standard procedure for the evaluation of the structure of a given material is the characterization by XRD (Fig. 7). In the present case, the calculation of the particle size using the Scherrer equation is pointless, as all the samples contained nanoparticles over 100 nm, which emerges from the interpretation interval of the Scherrer equation. Consequently, the only relevant information gained is the crystal phases present. In the case of the investigated samples (NP-1H, NP-1H-C, NP-5H, NP-5H-C, NP-24H,

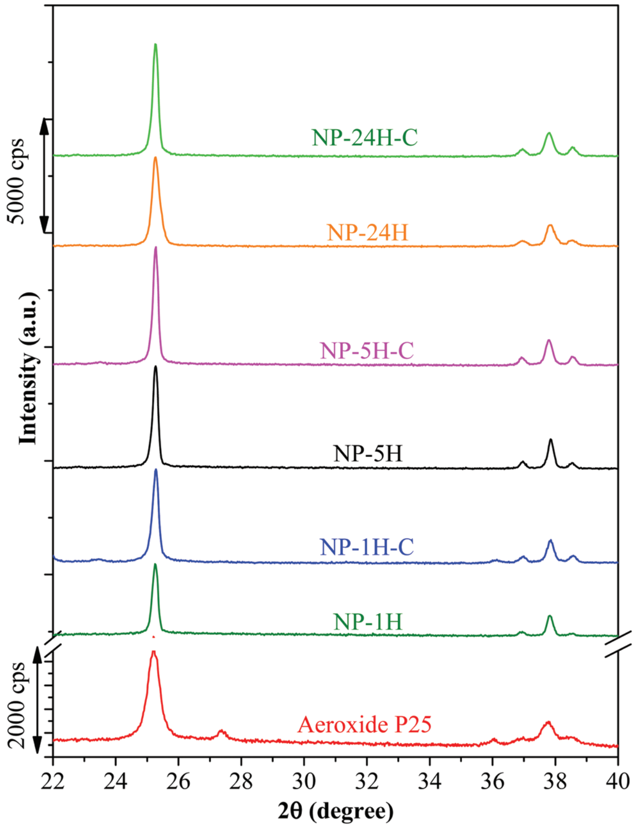

Fig. 7 XRD patterns of the obtained nanoplates and the reference photocatalyst Evonik Aeroxide P25.

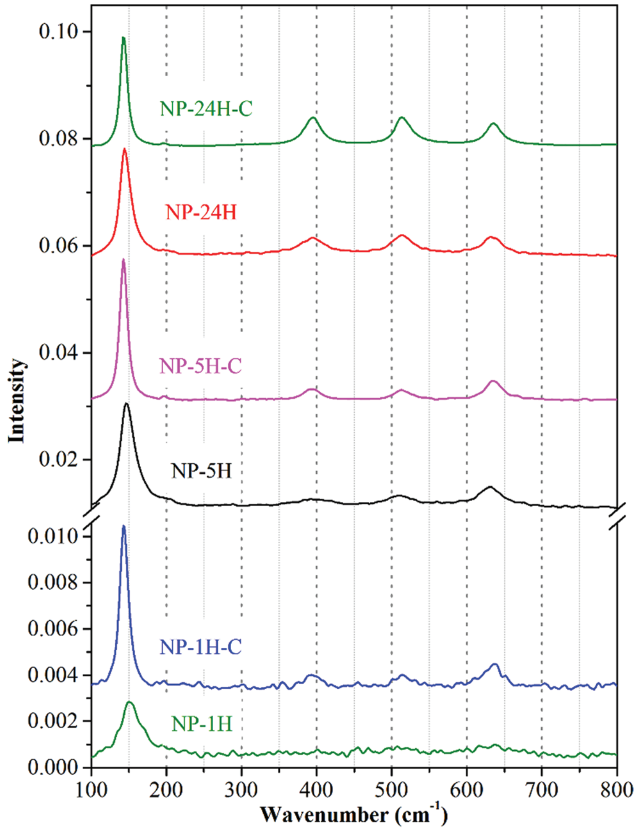

Fig. 8 Raman spectra of the obtained nanoplates. Note the different scale values on the vertical axis that were expressly added.

NP-24H-C) only the presence of anatase was detected, as expected from the nature of the applied synthesis procedure.[6]

However, crystallinity related information is always critical, considering the current circumstances, because sample NP-1H and sample NP-1H-C received only 1 hour of hydrothermal treatment. Hence, there is the possibility of having amorphous titania as well in the mentioned samples. If indeed that is the case, then these samples should be eliminated from photocatalytic activity tests. To elucidate this crucial issue Raman spectra were recorded. Fig. 8 reveals the presence of the bands characteristic for TiO_2 anatase located around 144, 394, 512 and 635 cm^{-1}, respectively.[35,36] However, as supposed, the crystallinity grade of the above mentioned samples is lower, especially for the sample NP-1H.

Taking into consideration that titania has a high Raman cross-section one can infer that the extremely low intensity recorded in the case of the two samples, *i.e.* NP-1H and NP-1H-C, in comparison with the other investigated ones shows the existence of a relatively significant amount of amorphous material. This excludes them from further testing for photocatalytic applications.

One can expect that these types of structural features can also induce changes in the optical properties of the materials. However, this was not the case, as shown in Fig. 9, where the first derivatives of the materials reflectance spectra were plotted. Furthermore, it was also clear that the scarce presence of carbon nanotubes does not influence the optical properties of the investigated materials.

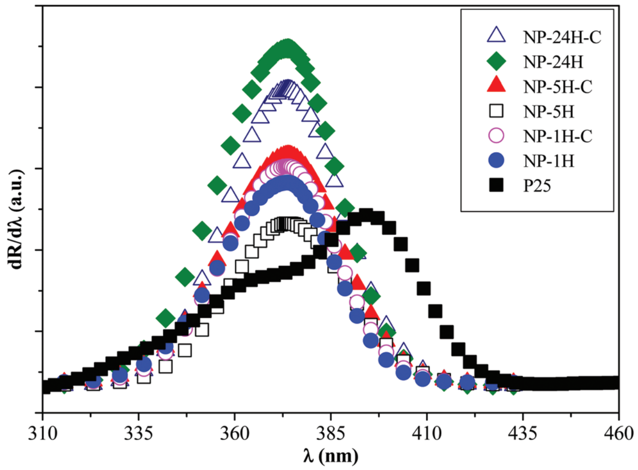

Fig. 9 The first derivative diffuse reflectance spectra of the investigated TiO_2 nanoplates.

The next method which could indicate the presence of the crystallographic holes are N_2 adsorption measurements. As the

Table 1 Photocatalytic performances and base parameters of the investigated nanoplates

Sample	Holes	C (wt%)	Surface normalized photocatalytic activity (mM min^{-1} m^{-2}) × 10^{-4}	Surface area (m^2 g^{-1})
P25	—	0	0.41	49.1
NP-1H	—	>50	—	—
NP-5H	—	2	5.81	0.57
NP-24H	—	2	6.16	0.49
NP-1H-C	Yes	>50	—	—
NP-5H-C	Yes	2	9.27	0.52
NP-24H-C	Yes	2	13.66	0.45

starting materials already contained relatively large crystallites an extremely low surface area was expected. Indeed, the obtained values were quite low and were presented in Table 1. Until now no clear signs have been detected which can indirectly confirm the presence of these interesting crystallographic holes.

However, their origin resides in the calcination procedure of the hydrothermally obtained nanoplates, which indicates that it is closely related to crystallization issues.[20,37] To follow this the Ti2p XPS spectra of all the samples were recorded and are presented in Fig. 10.

In the first instance the Ti2p$^{3/2}$ spectra of the non-heat-treated samples (NP-1H, NP-5H and NP-24H) was examined. A relatively small amount (0.35 at%) of Ti^{3+} was detected within these materials. However, the Ti^{3+} concentration did not change with the increase of the hydrothermal treatment duration. When the calcined materials (NP-1H-C, NP-5H-C and NP-24H-C) spectra were investigated, it was observed that, with the increase of the hydrothermal treatment time an increase of the Ti^{3+} amount was noticed, from 0.38 at% (NP-1H-C) to 0.57 at% (NP-5H-C), with the holes occurrence. As the holes performed the rotation (Fig. 4, sample NP-24H-C), the concentration of Ti^{3+} was nearly doubled, achieving a 1.1 at% value. The fact that the Ti^{3+} concentration does not increase with the hydrothermal treatment time in the case of the non-calcined samples (NP-1H, NP-5H and NP-24H), points out that the Ti^{3+} drastic increase, as obtained for the calcined samples (NP-1H-C, NP-5H-C and NP-24H-C), can most probably assigned to the presence/rotation of the holes.

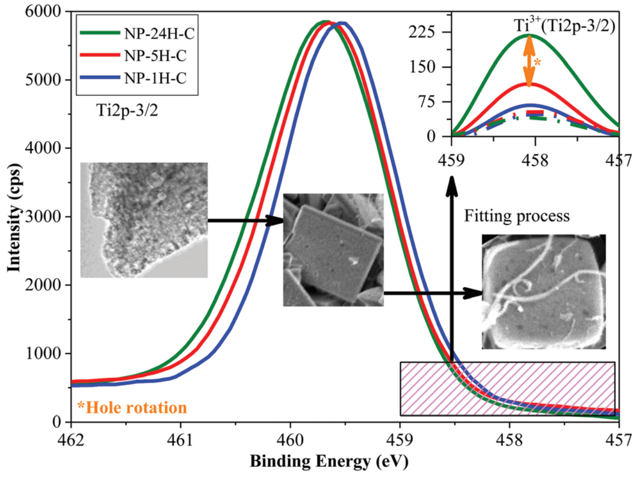

Fig. 10 Ti2p$^{3/2}$ spectra of the heat-treated photocatalysts, showing the shift of the spectrum towards higher binding energies, result that suggests the gradual appearance of Ti^{3+} (inset of Ti^{3+} component). The non-heat treated samples' (NP-1H, NP-5H and NP-24H) Ti^{3+} concentration was constant (marked with the dash/dot lines in the inset).

Mechanism of the hole formation: the relationship between: the concentration of Ti^{3+}↔presence of the holes↔hole rotation. As already stated in the previous sections of the paper an interesting correlation can be made between the presence/rotation of the holes and Ti^{3+} content. To understand this delicate relationship, the formation mechanism of the crystallographic holes should be discussed.

A short schematic overview of the proposed mechanism can be found in Fig. 11. The following facts should be taken into consideration:

(a) The titania microplates grow starting from the MWCNTs.

(b) The microparticles' (001) plane was "square" shaped, which suggests an equal growth speed of the facet in the directions D1, D2, D3 and D4 (Fig. 5).

(c) Based on be the 0 point of the crystallization direction is the centre of the facet.

During the calcination a recrystallization process was started, because the crystal gains excessive energy (heat). As the (001) plane is stabilized by the F$^-$ ions, the holes appear. By the presence of the holes the abundance of facet (001) was not lowered, because both at the "top" and the "bottom" of the

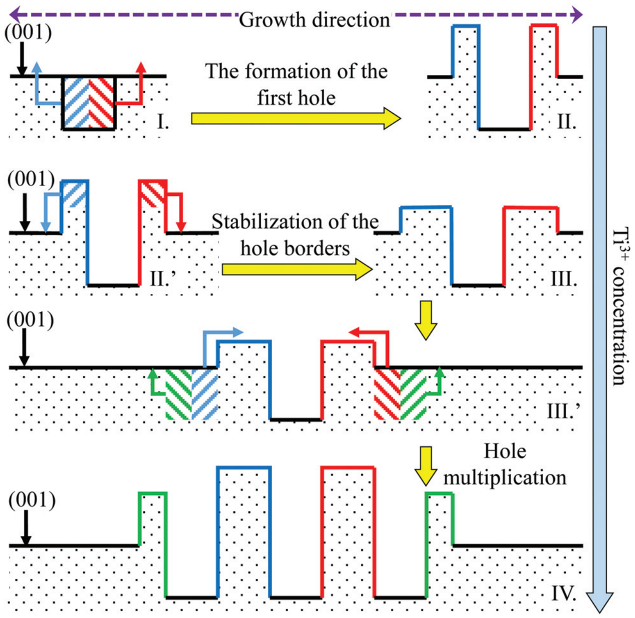

Fig. 11 The schematic representation of the proposed hole formation mechanism.

hole the same plane family is the dominant one. The mechanism involves three steps (Fig. 11):

(a) Appearance of the first hole (I→II).

(b) Stabilization of the hole borders (II′→III).

(c) Hole multiplication (III′→IV; in the ESI† the mechanism of the hole size distribution is also illustrated, Fig. S2).

Each of these steps involves a recrystallization process, which means that new edges/corners are generated raising the possibility for the appearance of crystal defects, evidenced (*via* XPS) by the presence of increased Ti^{3+} concentration.

As shown in Fig. 2, the faceting of the holes present in sample NP-24H-C was different, presenting a rotation compared to those observed in NP-1H-C and NP-5H-C. The {110} crystal facet (interior crystallographic plane of the rotated holes) has the highest surface energy among the low indexed crystallographic planes of titania and often appears at intermediate growth stages.[38] These type of facets (as they are transitory) multiply the already discussed recrystallization process' number. This means that with the appearance of the rotated holes the Ti^{3+} concentration increases as observed in the present case.

UV-light driven photocatalytic degradation of phenol

The photocatalytic activity of a given material can be analysed considering multiple facts and parameters. However, two approaches are emerging: the classical one, using weight normalized kinetic parameters or the surface normalized ones. Each approach has its own advantages and disadvantages. The authors choose to investigate the surface normalized values, because the present work focuses on the maximization of a specific crystallographic plane/decoration of these plains with "crystallographic holes".

In these studies, the samples NP-1H and NP-1H-C were not considered as their carbon content was too high to be compared with the other samples. Furthermore, these materials' crystallinity was also lower, which makes the comparison of the photocatalytic activities unreliable.

In the first approach the hydrothermal treatment time's effect was investigated. As the hydrothermal treatment time was prolonged the photocatalytic activity of the materials was nearly unchanged. However, with the appearance of the crystallographic holes, each of the studied catalysts' activity increased significantly (from 5.81×10^{-4} to 9.27×10^{-4} mM min^{-1} m^{-2} and from 6.16×10^{-4} to 13.66×10^{-4} mM min^{-1} m^{-2}) as shown in Table 1.

Furthermore, these activity values are far superior compared to the commercially available P25, namely a near 30 fold activity increase was achieved.

Additionally, if the samples NP-24H-C and NP-5H-C are compared then the first was 32% more active (Table 1 and Fig. 12) tended towards UV driven photocatalytic phenol degradation.

At first sight, the main morphological features which could be responsible for the activity are the presence/percentage of the exposed {001} facets and the appearance/rotation of the crystallographic holes. The first can be eliminated, as the percentage of the {001} crystallographic planes are nearly identical in the mentioned samples (73% NP-5H-C and 71% NP-24H-C – estimation based on data of 50 microcrystals from each sample).

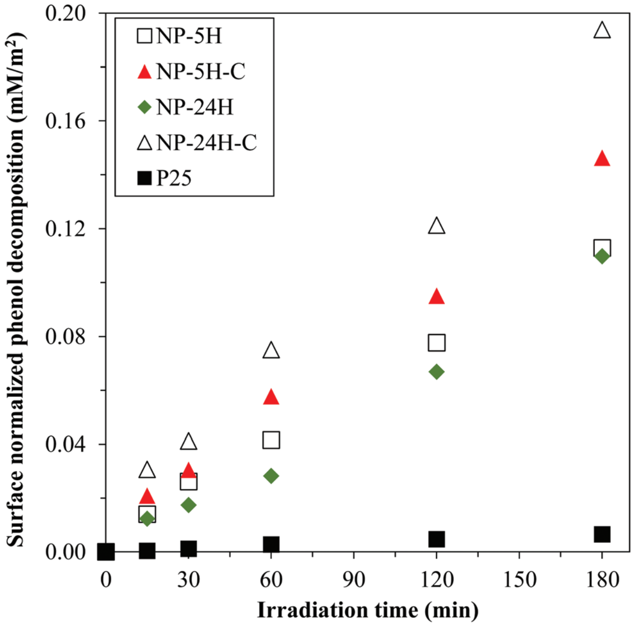

Fig. 12 The surface normalized photocatalytic activity of the obtained nanoplates for the degradation of phenol.

This is an important aspect because the only structural/morphological difference between these two samples was the presence of the rotated holes, meaning that their presence (the new orientation is marked by the blue crystallographic directions in Fig. 4) was beneficial for the activity of the titania nanoplates. Furthermore, with the appearance of the holes no relevant surface increase was noticed, reinforcing the facts listed above. Interestingly, with the appearance of the holes a higher quantity of Ti^{3+} was detected, while after the holes' rotation this value was further doubled. This is important, as Ti^{3+} centres are sometimes associated with O vacancies or even low binding energy oxygen types, which can enhance considerably photocatalytic activity.[30,31]

The high concentrations of Ti^{3+} present at the surface of the photocatalyst (due to the formation of the holes) are quite beneficial, as Ti^{3+} can react with the available dissolved O_2 (which was constantly assured in our experiments) and lead to the formation of reactive radicals, such as $^{\bullet}O_2^{-}$, $^{\bullet}HO_2$ and $^{\bullet}OH$[39] which are directly responsible for the degradation of the organic pollutants.

Furthermore, an activity increase through the enhanced adsorption of phenol on the surface of the titania can be excluded, as it is a poor adsorbing substrate. However, it is a critical issue in the case of good-adsorbing, low *vs.* high molecular weight pollutants, because the adsorption is critical and then the holes' supplementary area could also have an impact (low molecular weight pollutants – could easily enter even in the holes with $d < 5$ nm, *e.g.* salicylic acid – 5.8 Å; high molecular weighted pollutants – not using all the surface available through the holes, *e.g.* humic acid – molecular sizes >1 nm). The size of the phenol molecule is 4.2 Å.

It should be noted here that the obtained activity values show that the surface of these types of catalysts is far more active than the activity of the polycrystalline particles' surface. This result suggests that the controllability of the shape could represent a decisive factor for the activity enhancement of the semiconductor photocatalysts. If these shape factors (crystal shapes and crystallographic holes) could be implemented at lower particle sizes then highly active materials should emerge in the near future.

Experimental

Material synthesis

Synthesis of the titania microplates. In this case, after the hydrothermal treatment, no titania formation was noticed. 8 mL tetrabutyl titanate $Ti(OBu)_4$, was added into 104 mL HCl (5 M) solution, and then stirred for 30 min. A specific amount of HF (47%) was added to the mixture. After 5 min of continuous stirring the solution was transferred into a Teflon lined autoclave. In the meantime 15 mg of MWCNT was suspended in 40 mL of HCl (5 M), sonicated for 5 minutes and also added to the autoclave. The hydrothermal synthesis was conducted at 180 °C for 1, 5 and 24 h. Then, the autoclave was cooled down using a continuous water jet for 30 minutes. The composite materials were cleaned by centrifugation for 5 minutes in a 2 : 1 (v/v) mixture of 2-propanol and water. This purification step was repeated until the pH value of the supernatant was above 6. The obtained precipitate was redispersed in ultrapure water and dried at 80 °C for 24 h. All the samples (except those obtained after 1 hour of hydrothermal treatment) contained 2 wt% of C in their final mass.

The substrate dependence of the crystallization process is a well-known issue throughout the literature. To be absolutely sure that the obtained microcrystallites are formed only in the presence of the carbon nanotubes, the TiO_2 growth was verified without the carbon material.

Synthesis of the TiO_2 "holed" nanoplates. The desired amount of TiO_2 nanoplates was placed in a ceramic boat, which was introduced into a tubular furnace, supplied continuously with air (24 mL s^{-1}). Then the furnace was heated to 400 °C (10 °C min^{-1}) and maintained at this temperature for 2 h. The furnace was cooled down, using the same air supply. The samples were taken out, washed (as described in the previous section, but this time only water was used) and dried at 80 °C for 24 h. The carbon nanotube content was preserved as they are stable at the applied calcination temperature.

Sample nomenclature. The samples were coded as follows: NP-*x*H-C, where: NP stands for nanoplates, *x*H is the hydrothermal treatment time (*i.e.* 5H – 5 hours of hydrothermal treatment) and C indicates the heat treatment applied to the sample (calcination).

Material characterization

X-ray diffraction (XRD) measurements were performed on a Shimadzu 6000 diffractometer using Cu-Kα radiation (λ = 1.5406 Å), equipped with a graphite monochromator. The anatase – rutile phase ratio in P25 was evaluated using the Banfield's method,[40] and the crystallites' average size was calculated using the Scherrer equation.

FT-Raman spectra were recorded using a Bruker Equinox 55 spectrometer with an integrated FRA 106 Raman module using an Nd-YAG laser (1064 nm). Raman spectra were recorded with a spectral resolution of 1 cm^{-1}.

JASCO-V650 spectrophotometer with an integration sphere (ILV-724) was used for measuring the DRS spectra of the samples (λ = 300–800 nm). The possible electron transitions[41] were evaluated by plotting the $dR/d\lambda$ *vs.* λ, where R is the reflectance and λ is the wavelength.[20]

SEM-EDX analysis was performed on a Hitachi S-4700 Type II cold field emission scanning electron microscope equipped with a Röntec QX2-EDS spectrometer. No conductive coatings were applied on the samples so the fine morphological details could be observed.

The TEM samples were prepared by crushing in an agate mortar. The resulting powder was dispersed in ethanol and deposited onto Cu TEM grids provided with a holey *Formvar* membrane. The as-prepared samples were investigated using the JEM ARM 200F analytical TEM using selected area electron diffraction (SAED), conventional and high-resolution TEM (CTEM/HRTEM). The 3D projection of the particles was realized using ImageJ 1.47 software. The 3rd dimension was established taking into account the transmitted electron flux throughout the particle. The 0 level was then fixed at an electron density where no holes were observed on the microparticles.

XPS measurements were performed on a SPECS PHOIBOS 150 MCD instrument, with monochromatized Al Kα radiation (1486.69 eV) at 14 kV and 20 mA, and a pressure lower than 10^{-9} mbar. Samples were mounted on the sample holder using double-sided adhesive carbon tape. High-resolution Ti2p spectra were recorded in steps of 0.05 eV for the analysed samples. Analysis of the obtained data was carried out with CasaXPS software. All peaks were deconvoluted using Shirley background and Lorentzian–Gaussian line shapes. The applied value of the Gaussian–Lorentzian ratio was 30.

The surface areas of the obtained nanoplates were determined by N_2 sorption measurements performed with Sorptomatic 1990 equipment. The surface area was calculated by the Brunauer–Emmett–Teller (BET) 3 parameter method. The quantity of the samples was maximized as the investigated samples possessed an extremely low surface. By using this method the error of the measurement was kept as low as possible.

The assessment of the photocatalytic efficiencies: a photoreactor system with 3 × LighTech 60 W fluorescent lamps ($\lambda_{max} \approx 365$ nm, $d_{irradiation}$ = 5 cm, $t_{irradiation}$ = 3 hours) was used to measure the photocatalytic activities. The photocatalyst suspension containing phenol ($c_{0,\ \text{phenol}}$ = 0.5 mM, $c_{\text{suspension}}$ = 1.0 g L^{-1} composite, V_{susp} = 50 mL) was continuously purged by air in order to maintain the dissolved oxygen concentration constant during the whole experiment. The concentration decreases of the chosen organic substrate (phenol) and its degradation intermediates were followed using an Agilent 1100 series HPLC system. The assessed error of the photocatalytic tests (based on reproducibility experiments) was 4–7%. Due to the fact that the specific surface area of these materials was extremely low (around 0.5 m^2 g^{-1}, measured by N_2 adsorption), the decay curves were represented in surface normalized concentrations *vs.* time.

The molecular size (length) estimation of a given molecule was determined using CambridgeSoft ChemOffice 11.0.1.

Conclusions

Although the exact functioning/formation mechanisms of these intriguing crystallographic holes have not yet been clarified (although a possible formation mechanism was proposed in the present work), it is obvious that their potential in manipulating the properties of semiconductor oxides is remarkable. These results show that the future of the photocatalysis and photocatalysts' activity enhancement relies on three major factors. The first is the tailoring of the crystallite shape, as already described by several authors in the literature and by this the ratio of the different crystal facets. The second consists in the build-up of additional morphological elements, which can further increase the photocatalytic activity (*i.e.* as shown here – the presence of the crystallographic holes). The third, which still remains a challenge, is that the first and the second factors should be applicable also at lower particle sizes and with different materials.

Acknowledgements

The authors from Hungary would like to express their gratitude for the grant from Swiss Contribution (SH/7/2/20). The authors from Romania would like to thank the Romanian National Authority for Scientific Research, CNCS – UEFISCDI, project number PN-II-ID-PCE-2011-3-0442 for the financial support. Furthermore, the authors would like to express their gratitude to the funds received from the Romanian-Hungarian bilateral project nr. 661/2013/K-TÉT_12_RO-1-2013-0109966.

Notes and references

1 S. Li, J. Chen, F. Zheng, Y. Li and F. Huang, *Nanoscale*, 2013, **5**, 12150–12155.

2 S. Li, W. Liang, F. Zheng, X. Lin and J. Cai, *Nanoscale*, 2014, **6**, 14254–14261.

3 H. G. Yang, C. H. Sun, S. Z. Qiao, J. Zou, G. Liu, S. C. Smith, H. M. Cheng and G. Q. Lu, *Nature*, 2008, **453**, 638–641.

4 S. W. Yang and L. Gao, *J. Am. Ceram. Soc.*, 2005, **88**, 968–970.

5 J. G. Yu, G. H. Wang, B. Cheng and M. H. Zhou, *Appl. Catal., B*, 2007, **69**, 171–180.

6 J. Pan, G. Liu, G. Q. M. Lu and H.-M. Cheng, *Angew. Chem., Int. Ed.*, 2011, **50**, 2133–2137.

7 W. Wang, C. H. Lu, Y. R. Ni, F. P. Peng and Z. Z. Xu, *Appl. Surf. Sci.*, 2013, **265**, 438–442.

8 H. M. Li, Y. S. Zeng, T. C. Huang, L. Y. Piao and M. Liu, *ChemPlusChem*, 2012, **77**, 1017–1021.

9 R. Wanbayor and V. Ruangpornvisuti, *Appl. Surf. Sci.*, 2012, **258**, 3298–3301.

10 E. Burunkaya, M. Akarsu, H. E. Camurlu, O. Kesmez, Z. Yesil, M. Asilturk and E. Arpac, *Appl. Surf. Sci.*, 2013, **265**, 317–323.

11 Q. H. Chen, H. L. Liu, Y. J. Xin, X. W. Cheng and J. J. Li, *Appl. Surf. Sci.*, 2013, **264**, 476–484.

12 H. G. Yang, G. Liu, S. Z. Qiao, C. H. Sun, Y. G. Jin, S. C. Smith, J. Zou, H. M. Cheng and G. Q. M. Lu, *J. Am. Chem. Soc.*, 2009, **131**, 4078–4083.

13 Z. Y. Wang, K. L. Lv, G. H. Wang, K. J. Deng and D. G. Tang, *Appl. Catal., B*, 2010, **100**, 378–385.

14 Y. Zheng, K. Lv, Z. Wang, K. Deng and M. Li, *J. Mol. Catal. A: Chem.*, 2012, **356**, 137–143.

15 K. L. Lv, B. Cheng, J. G. Yu and G. Liu, *Phys. Chem. Chem. Phys.*, 2012, **14**, 5349–5362.

16 X. G. Han, Q. Kuang, M. S. Jin, Z. X. Xie and L. S. Zheng, *J. Am. Chem. Soc.*, 2009, **131**, 3152–3153.

17 X. L. Wang, H. L. He, Y. Chen, J. Q. Zhao and X. Y. Zhang, *Appl. Surf. Sci.*, 2012, **258**, 5863–5868.

18 K. X. Zhu, H. Y. Gao, G. X. Hu and Z. X. Shi, *J. Supercrit. Fluids*, 2013, **83**, 28–34.

19 J. G. Yu, G. P. Dai, Q. J. Xiang and M. Jaroniec, *J. Mater. Chem.*, 2011, **21**, 1049–1057.

20 G. Kovács, L. Baia, A. Vulpoi, T. Radu, É. Karácsonyi, A. Dombi, K. Hernádi, V. Danciu, S. Simon and Zs. Pap, *Appl. Catal., B*, 2014, **147**, 508–517.

21 É. Karácsonyi, L. Baia, A. Dombi, V. Danciu, K. Mogyorósi, L. C. Pop, G. Kovács, V. Coşoveanu, A. Vulpoi, S. Simon and Zs. Pap, *Catal. Today*, 2013, **208**, 19–27.

22 B. K. Vijayan, N. M. Dimitrijevic, D. Finkelstein-Shapiro, J. Wu and K. A. Gray, *ACS Catal.*, 2012, **2**, 223–229.

23 M. Takahashi, M. Inoue, R. Ihara, T. Yoko, T. Nemoto, S. Isoda, L. Malfatti, S. Costacurta and P. Innocenzi, *Adv. Mater.*, 2010, **22**, 3303–3306.

24 S. B. Yang, X. L. Feng and K. Mullen, *Adv. Mater.*, 2011, **23**, 3575–3579.

25 S. Li, J. Cai, X. Wu, F. Zheng, X. Lin, W. Liang, J. Chen, J. Zheng, Z. Lai, T. Chen and L. Zhu, *Appl. Catal., B*, 2014, **160–161**, 279–285.

26 V. R. Djokic, A. D. Marinkovic, O. Ersen, P. S. Uskokovic, R. D. Petrovic, V. L. R. Radmilovic and D. T. Janackovic, *Ceram. Int.*, 2014, **40**, 4009–4018.

27 Z. Ambrus, K. Mogyorósi, Á. Szalai, T. Alapi, K. Demeter, A. Dombi and P. Sipos, *Appl. Catal., A*, 2008, **340**, 153–161.

28 B. Ohtani, O. O. Prieto-Mahaney, D. Li and R. Abe, *J. Photochem. Photobiol., A*, 2010, **216**, 179–182.

29 T. Ohno, K. Sarukawa and M. Matsumura, *J. Phys. Chem. B*, 2001, **105**, 2417–2420.

30 Zs. Pap, É. Karácsonyi, Z. Cegléd, A. Dombi, V. Danciu, I. C. Popescu, L. Baia, A. Oszkó and K. Mogyorósi, *Appl. Catal., B*, 2012, **111–112**, 595–604.

31 Zs. Pap, V. Danciu, Z. Cegléd, Á. Kukovecz, A. Oszkó, A. Dombi and K. Mogyorósi, *Appl. Catal., B*, 2011, **101**, 461–470.

32 Y. Jo, I. Jung, I. Lee, J. Choi and Y. Tak, *Electrochem. Commun.*, 2010, **12**, 616–619.

33 Q. Wang, Z. H. Wen and J. H. Li, *Adv. Funct. Mater.*, 2006, **16**, 2141–2146.

34 K. Mogyorósi, E. Karácsonyi, Z. Cegléd, A. Dombi, V. Danciu, L. Baia and Zs. Pap, *J. Sol-Gel Sci. Technol.*, 2013, **65**, 277–282.

35 D. Georgescu, L. Baia, O. Ersen, M. Baia and S. Simon, *J. Raman Spectrosc.*, 2012, **43**, 876–883.

36 L. Baia, A. Peter, V. Cosoveanu, E. Indrea, M. Baia, J. Popp and V. Danciu, *Thin Solid Films*, 2006, **511–512**, 512–516.

37 L. Baia, A. Vulpoi, T. Radu, É. Karácsonyi, A. Dombi, K. Hernádi, V. Danciu, S. Simon, K. Norén, S. E. Canton, G. Kovács and Zs. Pap, *Appl. Catal., B*, 2014, **148–149**, 589–600.

38 G. Liu, H. G. Yang, J. Pan, Y. Q. Yang, G. Q. Lu and H. M. Cheng, *Chem. Rev.*, 2014, **114**, 9559–9612.

39 L.-B. Xiong, J.-L. Li, B. Yang and Y. Yu, *J. Nanomater.*, 2012, **2012**, 1–13.

40 H. Zhang and J. F. Banfield, *J. Phys. Chem. B*, 2000, **104**, 3481–3487.

41 D. Flak, A. Braun, B. S. Mun, J. B. Park, M. Parlinska-Wojtan, T. Graule and M. Rekas, *Phys. Chem. Chem. Phys.*, 2013, **15**, 1417–1430.